remote sensing

MDPI

Article

Characteristics and Tectonic Implications of the Geomorphic Indices of the Watersheds Around the Lijiang–Jinpingshan Fault

Yongqi Chen, Rui Ding *, Shimin Zhang, Dawei Jiang, Luyao Li and Diwei Hua

National Institute of Natural Hazards, Ministry of Emergency Management of China, Beijing 100085, China; chenyongqi22@mails.ucas.ac.cn (Y.C.)
* Correspondence: ruiding@ninhm.ac.cn

Abstract: The Lijiang–Jinpingshan fault (LJF) is an important secondary boundary fault that obliquely cuts the Sichuan–Yunnan rhombic block. It is of great significance for understanding the tectonic evolution of the Sichuan–Yunnan rhombic block and even the southeastern margin of the Tibet Plateau. Based on a digital elevation model (DEM), this work combines ArcGIS with MATLAB script programs to extract geomorphic indices including slope, the relief degree of the land surface (RDLS), hypsometric integral (HI), and channel steepness index (k_{sn}) of 593 sub–watersheds and strip terrain profiles around the LJF. By analyzing the spatial distribution characteristics of the geomorphic indices and combining the regional lithology and precipitation conditions, the spatial distribution of the geomorphic indices around the study area was analyzed to reveal the implications of the LJF's activity. The results of this work indicate that (1) the distribution of geomorphic indices around the LJF may not be controlled by climate and lithological conditions, and the LJF is the dominant factor controlling the geomorphic evolution of the region. (2) The spatial distribution patterns of geomorphic indices and strip terrain profiles reveal that the vertical movement of the LJF resulted in a pronounced uplift on its northwest side, with tectonic activity gradually diminishing from northeast to southwest. Furthermore, based on the spatial distribution characteristics of these geomorphic indices, the activity intensity of the LJF can be categorized into four distinct segments: Jianchuan–Lijiang, Lijiang–Ninglang, Ninglang–Muli, and Muli–Shimian. (3) The activity of the LJF obtained from tectonic geomorphology is consistent with the conclusions obtained in previous geological and geodesic studies. This work provides evidence of the activity and segmentation of the LJF in tectonic geomorphology. The results provide insight for the discussion of tectonic deformation and earthquake disaster mechanisms in the southeastern margin of the Tibet Plateau.

Keywords: Lijiang–Jinpingshan fault; tectonic implications; geomorphic indices; fault activity

Citation: Chen, Y.; Ding, R.; Zhang, S.; Jiang, D.; Li, L.; Hua, D. Characteristics and Tectonic Implications of the Geomorphic Indices of the Watersheds Around the Lijiang–Jinpingshan Fault. *Remote Sens.* **2024**, *16*, 3826. https://doi.org/10.3390/rs16203826

Academic Editors: Takashi Oguchi and Fumio Yamazaki

Received: 14 August 2024
Revised: 4 October 2024
Accepted: 12 October 2024
Published: 14 October 2024

1. Introduction

The southeastern margin of the Tibet Plateau is a hotspot for studying the current crustal deformation pattern and tectonic evolution of the Tibet Plateau because of strong tectonic activity [1]. The Sichuan–Yunnan rhombic block is a part of the eastward extrusion of material from the Tibet Plateau and plays an important regulatory role in the diffusion of material on the southeastern margin of the Tibet Plateau [2,3]. The NE trending Lijiang–Jinpingshan fault (LJF) is a transverse fault that cuts across the Sichuan–Yunnan rhombic block and is an important component of the southeastern boundary of the Tibet Plateau. Studies have shown that, since the Pliocene, the southeastward slip of the Tibet Plateau has been mainly adjusted by large–scale left–lateral strike–slip of the Xianshuihe fault and the LJF and the clockwise rotation of the Sichuan–Yunnan rhombic block [4]. Therefore, studying the activity characteristics of the LJF is of great significance for understanding the tectonic evolution of the Sichuan–Yunnan rhombic block and even the southeastern Tibet Plateau.

Tectonic geomorphology is an emerging interdisciplinary field in recent years that combines geomorphology and structural geology [5]. It aims to understand the interaction between tectonic processes and landforms on a specific regional scale by describing the landscape characteristics of the surface [6,7]. Tectonics is important in driving landform evolution and affecting surface processes. The current landforms result from the combined effects of tectonics and erosion [8]. In areas with active tectonics, the landform development within the watershed is sensitive to controlling factors such as tectonic uplift, climate, and lithology. The development and evolution of the rivers within the watersheds record information on changes in tectonics and climate [9]. The geomorphic index is a quantitative expression of surface characteristics and a powerful tool for inverting the history, amplitude, and rate of tectonic activity. It can reveal information on tectonic activities at time scales ranging from tens of thousands to millions of years and is particularly suitable for areas with large tectonic differences and strong tectonic uplift. The watershed is an ideal place to understand the response relationship between tectonics, geomorphology, and river systems [10,11]. Nowadays, with the advancement of GIS and the gradual refinement of high–resolution digital elevation models (DEMs) [12], it is increasingly easy to study tectonic activities through geomorphic indices and achieve remarkable results [13–15].

The purpose of this study is to evaluate the response of geomorphic indices to LJF activity. The paleoearthquake history [16,17] and slip rate [18–21] of the central and southern sections of the LJF indicate strong tectonic activities. Previous studies have mainly focused on geology, geophysics, and geodesy. Areas where the geomorphic features of the two sides of a fault are significantly different due to normal or thrust faults are more suitable for applying geomorphic indices for tectonic geomorphological research. The most typical geomorphic feature of this pattern is high mountains on one side of the fault and a basin on the other side [13], which is called a basin–mountain pattern. Although the LJF is a left–slip and thrust fault, the area around the LJF is not a typical basin–mountain pattern, making it very difficult to conduct geomorphic index research. Currently, there are very few studies on geomorphic indices in this area, and the only research is limited to the central and southern sections of the LJF [22], so it is crucial to conduct geomorphic index research on the entire fault. Based on the DEM, obtained using the US SRTM (Shuttle Radar Topography Mission) program and named SRTM–1, we extracted and analyzed the spatial distribution characteristics of geomorphic indices (slope, relief degree of the land surface (RDLS), hypsometric integral (HI), and channel steepness (k_{sn})) using ArcGIS and MATLAB tools. Furthermore, we evaluated the response of geomorphic indices to LJF activity in combination with the spatial distribution of regional lithology and precipitation.

2. Regional Geological Overview

The southwest border of the LJF is the Jianchuan basin in the north of the Red River fault, and it moves NE through Lijiang, Yanyuan, etc. After passing Muli, it turns NNE and intersects with the Anning River fault near Shimian (Figure 1). The terrain on both sides of the LJF is significantly different: the terrain on the northwest side of the LJF is steep, mostly mountainous and canyon areas, while the terrain on the southeast side is relatively flat, with many basins. Most geological [19,21,23] and geodetic [18,24] studies have shown that the LJF is a high–angle reverse fault with an NW–dipping, left–lateral strike–slip. According to the activities and geometric characteristics of the LJF, previous researchers divided it into northeast, middle, and southwest segments, with Lijiang and Muli as the boundaries [16].

The LJF obliquely cuts the Sichuan–Yunnan rhombic block, which constitutes the southwestern segment of the Mesozoic–Cenozoic nappe tectonic belt spanning Longmen Mountain, Jinping Mountain, and Yulong Mountain [1,25,26]. In this fault zone, a large–scale left–lateral strike–slip initiated in the Late Pliocene or the Early Pleistocene, and vertical dislocation began in the Middle Pleistocene [4]. It has remained strongly active since the Quaternary [27,28]. The strata around the LJF are well developed, with pre–Cenozoic strata ranging from the Sinian to the Jurassic, while the Cretaceous is absent. The Paleozoic

strata northwest of the LJF are well–developed, thick, and mainly shallow marine facies deposits. To the southeast of the LJF, the strata thickness gradually becomes thinner, which is dominated by coastal facies, but the Paleozoic strata are largely missing [29]. As an important boundary fault, strong earthquakes frequently occur around the LJF. According to the Chinese Historical Earthquake Catalog released by the National Earthquake Data Center: https://data.earthquake.cn/datashare/report.shtml?PAGEID=earthquake_zhengshi (accessed on 10 November 2023), there have been 35 destructive earthquakes (M > 5.0) within 20 km around the LJF, including 10 earthquakes with M > 6.0. The largest earthquake, M = 7.0, occurred in Lijiang on 3 February 1996.

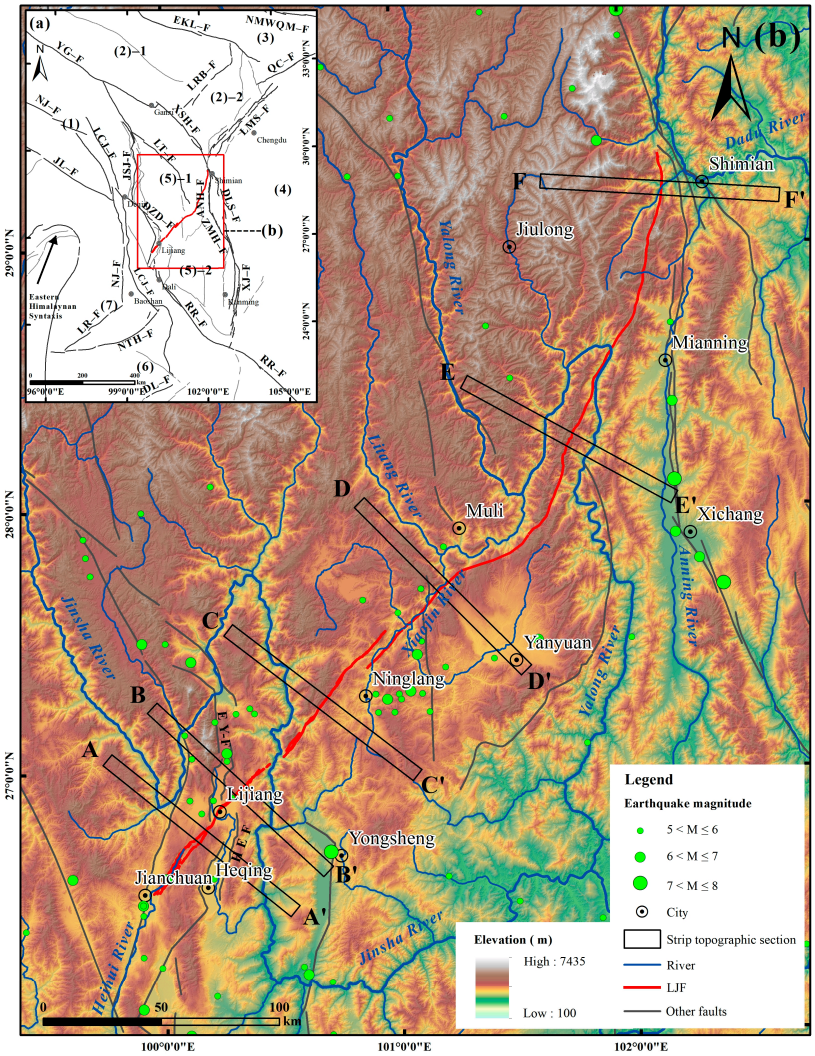

Figure 1. The geological map of the study area. (**b**) is the red frame range in (**a**). (**a**) The main active faults in the southeastern margin of the Tibetan plateau. (**b**) The geometric distribution of the LJF and introduction of the study area. A–A′ to F–F′ are strip terrain profiles. (1): Qiangtang block, (2)–1: Aba sub–block, (2)–2: Longmenshan sub–block, (3): Chaidamu block, (4): South China block, (5)–1: Northwestern Sichuan sub–block, (5)–2: Central Yunnan sub–block, (6): Jinggu–Ximeng block, (7): Baoshan sub–block, EKL–F: East Kunlun fault, NMWQM–F: North margin of the West Qinling Mountains fault, LRB–F: Longriba fault, MJ–F: Minjiang fault, LMS–F: Longmenshan fault, QC–F: Qingchuan fault, YG–F: Yushu Ganzi fault, XSH–F: Xianshuihe fault, ANH–F: Anninghe fault, ZMH–F: Zemuhe fault, DLS–F: Daliangshan fault, XJ–F: Xiaojiang fault, LT–F: Litang fault, JSJ–F: Jinshajiang fault, DZD–F: Deqin Zhongdian Daju fault, RR–F: Red River fault, NJ–F: Nujiang fault, DL–F: Daluo fault, NTH–F: Nantinghe fault, LR–F: Longling Ruili fault, H E–F: Heqing Eryuan fault, E Y–F: Eastern Piedmont fault of the Yulong Mountains.

3. Data and Methods

3.1. Data

The DEM used in this work is SRTM–1, obtained from the United States' SRTM program (Shuttle Radar Topography Mission), with a resolution of 30 m. SRTM utilizes interferometric synthetic–aperture radar (InSAR) technology to collect a global DEM, which provides high–precision data for global–scale topographic and geomorphological research. SRTM can obtain better surface data in mountainous areas with thick vegetation [30,31]. The precipitation data come from the monthly precipitation data of China from 1901 to 2022 [32], published at the Tibetan Plateau Data Center, with a resolution of 1 km. Due to the influence of data accuracy, this work selected precipitation data from 2000 to 2022 only and performed spatial analysis in ArcGIS to obtain the average annual precipitation (AAP). The lithology data are based on the published 1:2.5 million geological maps of China [33]. To obtain the rock hardness (RH) value of the study area, we assigned the RH according to the lithology and age. Finally, the average RH of the sub–watersheds of the study area was obtained through spatial analysis in ArcGIS.

3.2. Extracting Watersheds

The southern end of the LJF belongs to the Heihui River basin, which flows into the Lancang River. Except for the southern end, the rest belongs to the Yangtze River basin (Figure 2). Field investigations and related studies have shown that most of the riverbed in the study area is bedrock, and part of the riverbed is covered by a thin layer of clastic sediments [34]. In addition, there are landslides, collapses, and debris flows at the headwaters of some rivers. According to relevant studies, debris flows in bedrock mountain areas mainly occur in areas with a catchment area of <1 km^2, and this value is defined as the critical catchment area for the transition from a colluvial area dominated by debris flows to a bedrock river [35]. Previous studies have shown that setting the catchment area to 10 km^2 on the eastern side of the Tibet Plateau can eliminate the impact of the colluvial zone [36,37]. In addition, the calculation of k_{sn} based on the river hydraulic erosion model should be based on bedrock rivers and bedrock watersheds. Therefore, non–bedrock rivers and areas greatly affected by humans should be excluded when extracting watersheds. To summarize the above requirements, this work utilized the ArcGIS software (version 9.2) to extract the watersheds with a catchment area greater than 10 km^2 in the study area. It obtained 593 bedrock river watersheds, which are located on both sides of the main rivers around the LJF (Figure 2).

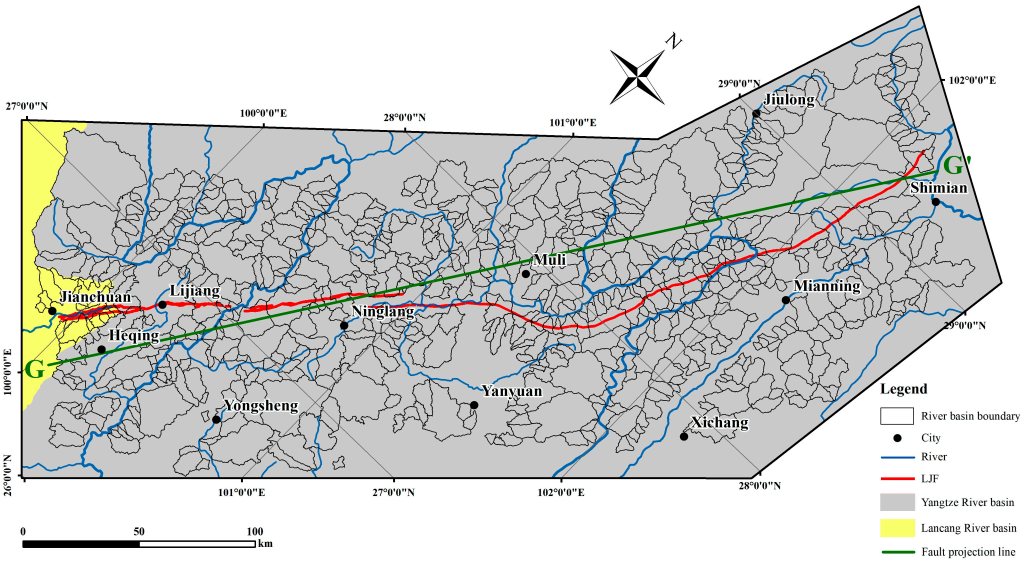

Figure 2. The results of watershed extraction in the study.

3.3. Geomorphic Indices

3.3.1. Slope and Relief Degree of the Land Surface (RDLS)

The slope represents the inclination of the Earth's surface [38], a common indicator reflecting the tectonic geomorphic conditions of bedrock mountainous areas. The slope can be obtained through the relationship between a grid in the DEM and its eight surrounding neighborhood grids. Previous studies have shown that the slope has a certain critical value, about 30° [39]. Beyond 30°, the slope will no longer increase with the increase in the erosion rate, and geological disasters such as landslides and collapses are very likely to occur [40,41].

RDLS is the difference between the maximum and minimum elevation values within a certain area, representing the degree of incision and erosion. The surface in the early stages of evolution has a more significant elevation difference, while the older surface has a smaller relief due to long–term leveling processes. The intensity of surface incision and erosion is closely related to the strength of tectonic activity. Therefore, RDLS can indirectly reflect the strength of tectonic activity [42]. Local RDLS is often used in applications, which can be obtained by calculating the difference between the maximum and the minimum elevation value around a specific grid through the analysis window (Figure 3). Experiments have shown that local RDLS has a scale effect. The size of the analysis window directly affects the accuracy and macroscopic reflection of RDLS. As the analysis window gradually increases, the relative height difference increases. However, when the analysis window expands to a certain extent, the growth rate of RDLS slows. The corresponding analysis window size is the optimal analysis scale [43,44]. The size of the optimal analysis window varies with the data and resolution. Referring to previous studies on selecting the optimal analysis window [45,46], this work selects the analysis window of 50 × 50 grid cells based on the SRTM–1 data.

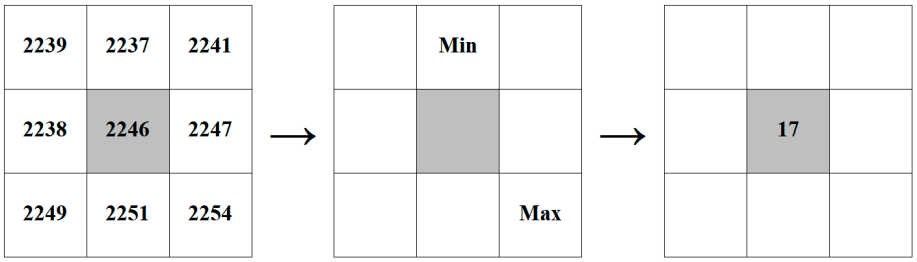

Figure 3. The calculation principle of the analysis window (taking a 3 × 3 size as an example).

3.3.2. Hypsometric Integral (HI)

Strahler proposed using the HI of river watersheds to reflect the geomorphic development characteristics, and the value of HI ranges from 0 to 1 [47]. According to Davis's geomorphic erosion cycle theory, geomorphic evolution can be divided into juvenile (HI > 0.5), mature (0.5 ≥ HI > 0.4), and old stages (HI ≤ 0.4) [48]. The corresponding basin area–elevation integral curves are convex, S–shaped, and concave, respectively, and the HI changes from large to small. Generally speaking, the longer the landform evolution time, the higher the degree of erosion. After the original geological body is weathered, eroded, and transported, the volume remaining in the original place is smaller, and the area–elevation integral curve evolves from the initial convex type to the concave type, and the HI gradually decreases [49]. If the tectonic activity in a region is strong, it is difficult for the landform evolution to reach a balanced state. The strong vertical activity will keep the watersheds in the juvenile or mature stage, and the HI will maintain a very high value. Therefore, HI is very sensitive to tectonic differences and can indirectly reflect the degree of the vertical uplift of tectonics.

According to Pike's research results [50], in practical applications, the HI calculation formula of a watershed can be simplified to

$$\mathrm{HI} = \frac{H_{mean} - H_{min}}{H_{max} - H_{min}} \quad (1)$$

In Formula (1), H_{max} is the maximum elevation in a specific watershed, H_{min} is the minimum elevation in a specific watershed, and H_{mean} is the average elevation in a specific watershed.

3.3.3. Channel Steepness Index (k_{sn})

The hydraulic erosion model under a steady–state river channel links the bedrock channel uplift rate with the channel erosion rate and uses the concavity index and k_{sn} to characterize the relative strength of tectonic uplift. The bedrock uplift rate is high in areas with a large channel gradient and steep slope, and it is low in areas with a small channel gradient and gentle slope [51]. Bedrock channels are very common in areas with intense tectonic activity, such as the Southeastern Tibet Plateau. In tectonic uplift areas, since the elevation change in the river longitudinal profile is the result of competition between bedrock uplift and channel erosion and incision, the elevation change (z) of a certain point in the channel within a certain time (t) is jointly determined by the rock uplift rate (U) and the erosion rate (E) [42,52], which can be expressed by Formula (2):

$$\frac{\partial z}{\partial t} = U(x,t) - K(x,t)A(x,t)^m \left|\frac{\partial z}{\partial x}\right|^n, \quad (2)$$

In Formula (2), K is the erosion coefficient, A is the catchment area, m is the area index, n is the slope index, and x is the horizontal distance from a point to the upstream of the river. In $z = Sx$, where S is the slope of the river at that point. The hydraulic erosion model assumes that the river is in steady state, at which time the elevation of a point in the river will no longer change with time—that is, $z/t = 0$, and Formula (2) is transformed into

$$0 = U - KA^m S^n, \quad (3)$$

Formula (2) can further be transformed into

$$S = \left(\frac{U}{K}\right)^{\frac{1}{n}} A^{-\frac{m}{n}}, \quad (4)$$

If $k_{sn} = \left(\frac{U}{K}\right)^{\frac{1}{n}}$, $\theta = \frac{m}{n}$, Formula (4) is transformed into

$$S = k_{sn} A^{-\theta}, \quad (5)$$

In Formula (5), k_{sn} is the channel steepness index and $A^{-\theta}$ is the concavity index [53].

Formula (5) is the same as the power function relationship between the river slope (S) and the catchment area (A) [54]. When comparing Formulas (4) and (5), when K and n are constants, U positively correlate with k_{sn}, so the k_{sn} value can reflect the tectonic uplift. The steeper the river slope in a certain area, the higher the k_{sn} value, and the stronger the tectonic uplift in the area [40].

3.4. Strip Terrain Profiles

When terrain analysis is performed based on a DEM, the elevation profile can directly reflect the elevation changes in the terrain surface. However, the traditional single profile line is highly subjective when selecting the location, and the results are not convincing [12]. Strip terrain profiles can obtain the maximum, minimum, and average values of terrain elevation within a certain width, which effectively avoids the accidental results of a single profile [55,56]. The differential uplift of the two sides of a fault caused by tectonic activity

can be reflected in the strip terrain profile [57,58]. In this study, six strip terrain profiles were evenly selected perpendicular to the fault in the southern, middle, and northern sections of the LJF, each with a width of 6 km and a length of 100 km (Figure 1).

3.5. Correlation Analysis

Pearson and Spearman correlation are the main methods of correlation analysis. The applicable conditions of the two methods differ. If the data follow a normal distribution, the Pearson correlation coefficient is used to study the relationship between parameters; otherwise, the Spearman correlation coefficient is used [59]. The data of this study obviously do not follow a normal distribution. The Spearman correlation coefficient uses a monotone equation to evaluate the correlation between X (independent variable) and Y (dependent variable). When X increases, Y also tends to increase, and the Spearman correlation coefficient is greater than 0 and less than 1, indicating a positive correlation. When X increases, Y tends to decrease, and the Spearman correlation coefficient is greater than –1 and less than 0, indicating a negative correlation. The correlation coefficient of 0 indicates that there is no correlation between X and Y. The Spearman correlation coefficient is calculated as follows (Equation (6)):

$$\rho = 1 - \frac{6\sum_{i=1}^{n} d_i^2}{n(n^2-1)}, \quad (6)$$

where ρ represents the correlation coefficient, d_i represents the grade difference between X and Y, and n represents the number of samples.

4. Results

4.1. The Result of Slope and Relief Degree of the Land Surface (RDLS)

The spatial distribution of the slope (a) and RDLS (b) around the LJF is shown in Figure 4. The spatial distributions of the two are very similar. Perpendicular to the strike direction of the LJF, the slope and RDLS in the northwest of the LJF are significantly higher than those in the southeast; along the strike direction of the LJF, the slope and RDLS on both sides of the LJF show a trend of low in the southwest and high in the northeast. For example, the slope and RDLS around the Lijiang, Yanyuan, and Mianning basins are low–value areas. In addition, the slope and RDLS on both sides of most rivers are higher than those in other regions, especially in RDLS.

Via spatial analysis in ArcGIS, the spatial distribution results of the geomorphic indices of 593 sub–watersheds around the LJF were obtained. The vector surface elements of the sub–watersheds were converted into points using spatial analysis tools, and the sub–watersheds were divided into the northwest and southeast sides of the LJF according to their positions after point conversion. Among them, 304 sub–watersheds belonged to the northwest side, and 289 sub–watersheds belonged to the southeast side (see Supplementary Materials).

The spatial distribution of the average slope (a) and RDLS (b) of the sub–watersheds is shown in Figure 5. The average slope of the sub–watersheds ranges from 6.5 to 41°, and the RDLS ranges from 345 to 4695 m. According to statistics, the average slope of 304 sub–watersheds on the northwest side of the LJF is 27.47°, and the average slope of 289 sub–watersheds on the southeast is 24.2°; the average RDLS of the sub–watersheds on the northwest is 2067.93 m, and the average RDLS on the southeast is 1667.29 m (Table 1). Therefore, the slope and RDLS on the northwest side of the LJF are higher than those on the southeast. Similar to the whole region, the spatial distribution of the slope and RDLS in the sub–watersheds also shows a trend of being high in the northwest and low in the southeast perpendicular to the fault strike and high in the northeast and low in the southwest along the fault strike. However, unlike the whole region, the slope and RDLS of the sub–watersheds have an obvious high–value area in the north of Lijiang, which may be affected by the Eastern Piedmont fault of the Yulong Mountains (Figure 1) [60,61]. In addition, after rivers in the dashed black area cross the LJF, the slope and RDLS value of the sub–watersheds on both sides of the river are significantly reduced. Without considering

other factors, the spatial distribution results of the slope and RDLS on both sides of the LJF reflect the strong tectonic uplift in the northwest of the LJF and the trend of the fault activity gradually decreasing toward the southwest.

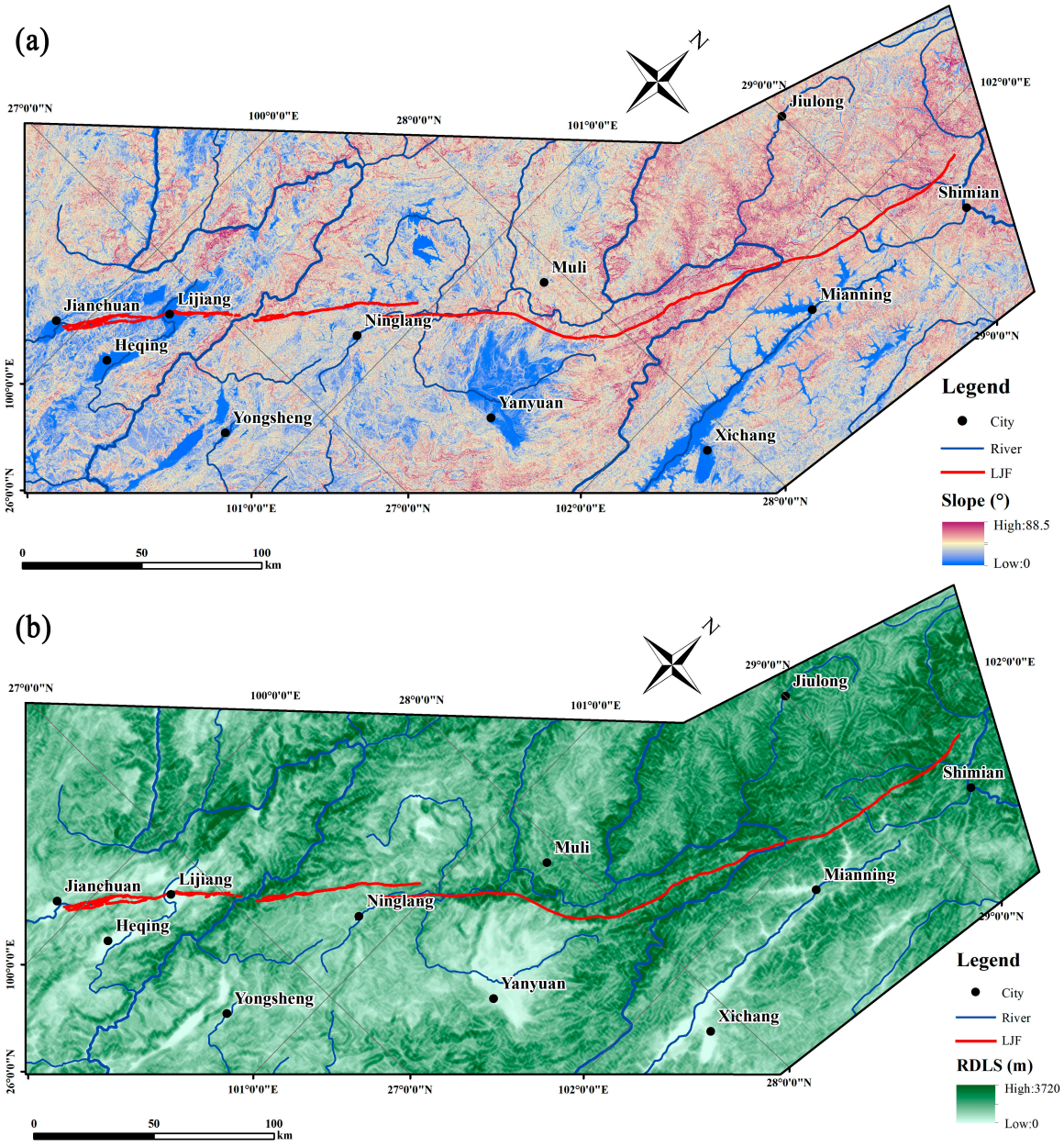

Figure 4. The slope (**a**) and RDLS (**b**) distribution around the LJF.

Table 1. The mean values of geomorphic indices, AAP, and RH of sub–watersheds on both sides of the LJF.

	AAP	Slope	RDLS	HI	k_{sn}–YT	k_{sn}–LC	RH
NW	675.40	27.47	2067.93	0.5380	50.28	39.43	27.89
SE	716.54	24.20	1667.29	0.4901	36.84	36.23	28.64

Note: AAP: average annual precipitation, RH: rock hardness, YT: Yangtze River, LC: Lancang River.

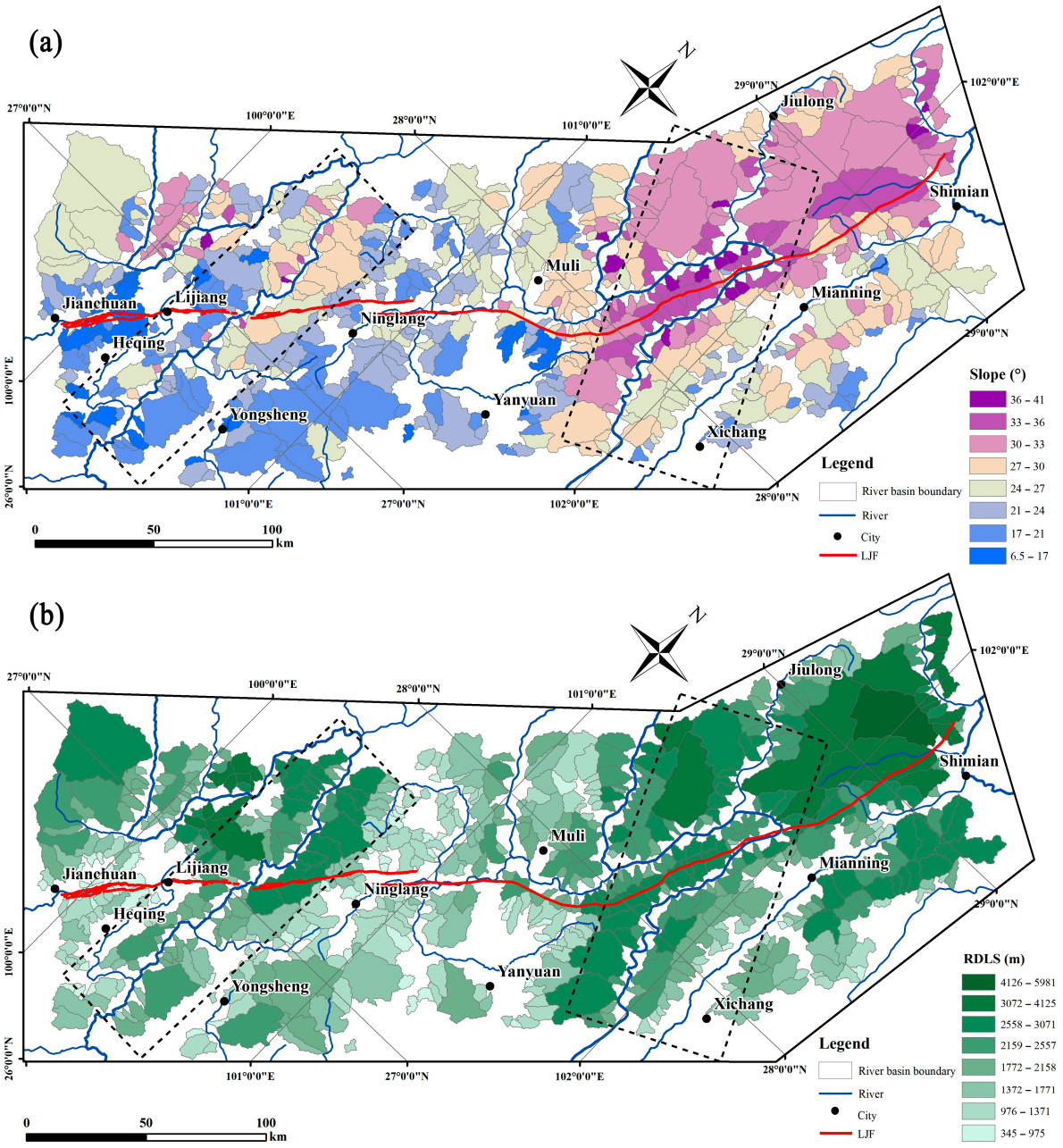

Figure 5. The spatial distribution of the average slope (**a**) and RDLS (**b**) in the sub–watersheds around the LJF.

4.2. The Result of Hypsometric Integral (HI)

Figure 6 shows the spatial distribution of HI in the sub–watersheds. The HI values of the watersheds range from 0.22 to 0.74. The detailed values of the HI are shown in Supplementary Materials. According to the statistics, the average HI of the sub–watersheds on the northwest side of the LJF is 0.54, and the average HI on the southeast is 0.49 (Table 1).

According to statistics, the number of sub–watersheds with an HI higher than 0.5 on the northwest side of the LJF accounts for 71% of the total number on the northwest side, while only 45% are located on the southeast side. HI values higher than 0.5 indicate that the sub–watersheds on the northwest side of the LJF are in their juvenile stage [48]. If other factors are not considered, this can indirectly reflect the strong tectonic uplift in the northwest of the LJF. Based on the results of the Spearman correlation analysis, the correlation between HI and other geomorphic indices is weak. The spatial distribution of

HI shows that the HI on the northwest side of the LJF is higher than that on the southeast, but the variation trend of HI along the fault direction is not obvious. In this work, the performance of HI on the difference in geomorphic features is weaker than other indices, which may be due to the use of the simplified HI formula. Although the variation trend of HI along the fault direction on the southeast side is not obvious, the HI on the northwest side decreases toward the southwest, which reflects that the tectonic uplift of the LJF gradually weakens toward the southwest.

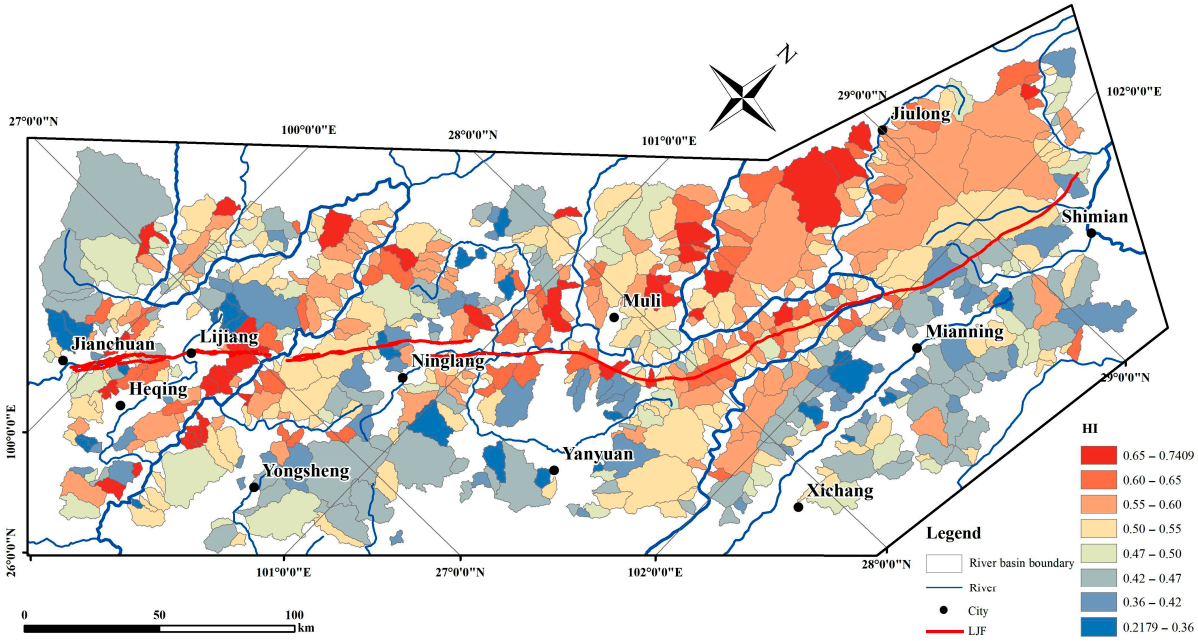

Figure 6. The spatial distribution of HI in the sub–watersheds around the LJF.

4.3. The Result of Channel Steepness Index (k_{sn})

There are many methods that can be used to calculate k_{sn} [62]. We utilized the Topo-Toolbox program written by Schwanghart and colleagues based on MATLAB to calculate the k_{sn} of the channels in this work [63,64]. This method can obtain the k_{sn} of the channels in the largest watershed within the data range. Since the LJF spans the Yangtze River and Lancang River basins (Figure 2), it is necessary to process the DEM separately to obtain the k_{sn} of the channels in the two basins. Due to the amount of data, only part of the k_{sn} is shown in Figure 7b,c.

Figure 7a shows the spatial distribution of the mean k_{sn} of the sub–watersheds. The detailed values of the mean k_{sn} of each sub–watershed are shown in Supplementary Materials. The statistics show that, in the Yangtze River basin, the average k_{sn} of the sub–watersheds in the northwest of the LJF is 50.28, and the average k_{sn} in the southeast is 36.84, much smaller than that in the northwest. In the Lancang River basin, although fewer watersheds are selected, the average k_{sn} of the sub–watersheds in the northwest is 39.43, and the average k_{sn} of the sub–watersheds in the southeast is 36.23, which is also smaller than that in the northwest. The spatial distribution characteristics of k_{sn} are very similar to the slope and RDLS, showing that perpendicular to the fault direction, the average geomorphic indices of sub–watersheds in the northwest are higher than that in the southeast, and the geomorphic indices on both sides of the LJF decrease from northeast to southwest. After rivers cross the LJF in the dashed black area in Figure 7a, the k_{sn} of the sub–watersheds on both sides also decrease significantly toward the southeast. Without considering other factors, the spatial distribution results of k_{sn} also confirm that the tectonic uplift in the northwest of the LJF is stronger than that in the southeast, and the intensity of fault activity decreases toward the southwest.

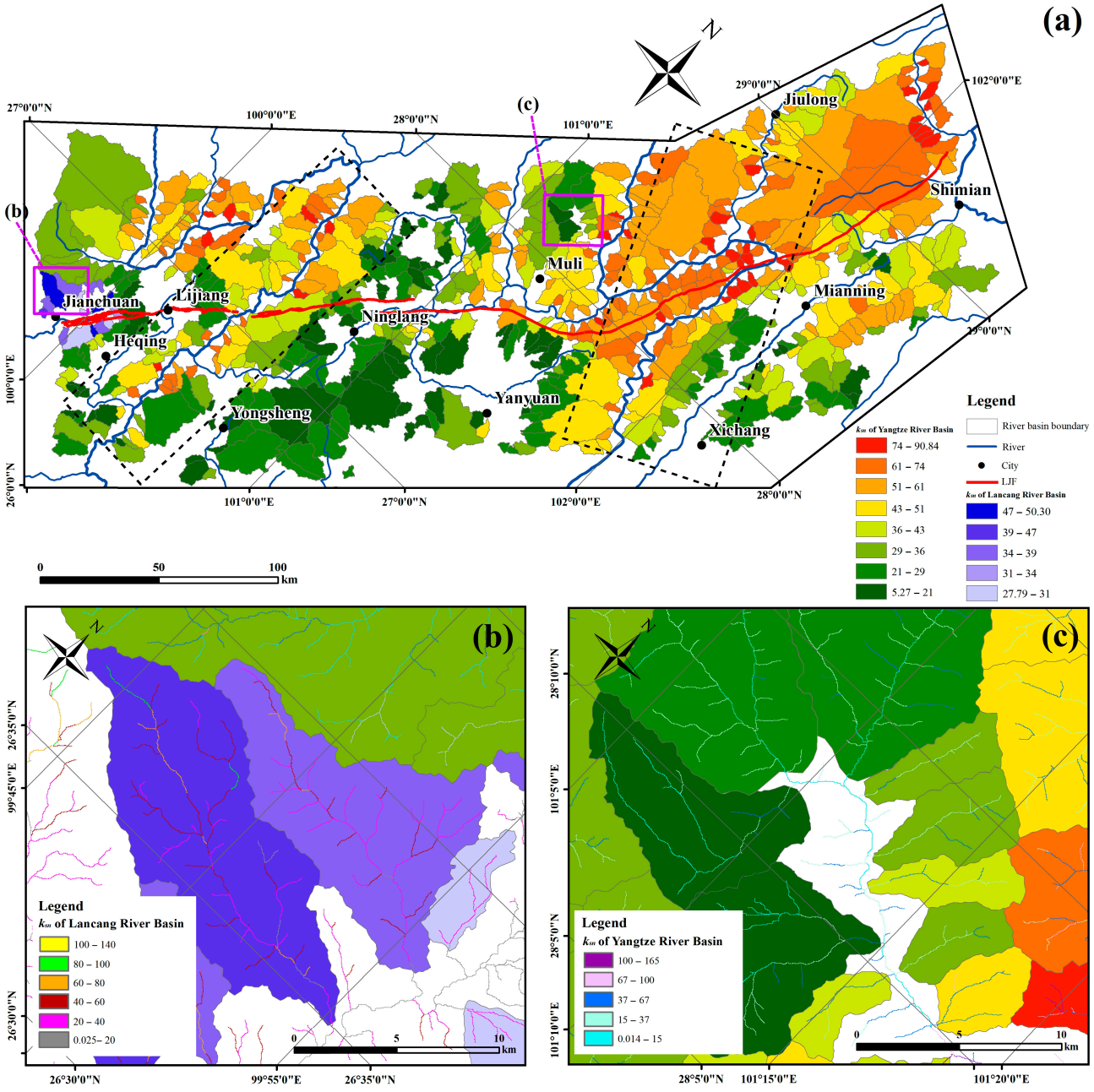

Figure 7. The spatial distribution of the average k_{sn} in the sub–watersheds around the LJF. (**b**,**c**) are the purple frame areas in (**a**). (**b**) is a display of k_{sn} in the Lancang River Basin. (**c**) is a display of k_{sn} in the Yangtze River Basin.

4.4. The Result of Strip Terrain Profile

The strip terrain profiles from A–A′ to F–F′ (Figure 1) reflect the variations in elevation perpendicular to the fault direction. The strip terrain profiles have obvious tectonic uplift responses at the LJF except for A–A′, and the topography of the two sides of the LJF is significantly different (Figure 8). If other factors are not considered, the results show that to the east of the Lijiang basin, the tectonic uplift on the northwest side of the LJF is stronger than that in the southeast. We also observed that the average elevation from A–A′ to F–F′ profiles increases, which further indicates that the vertical activities of the LJF increase from southwest to northeast.

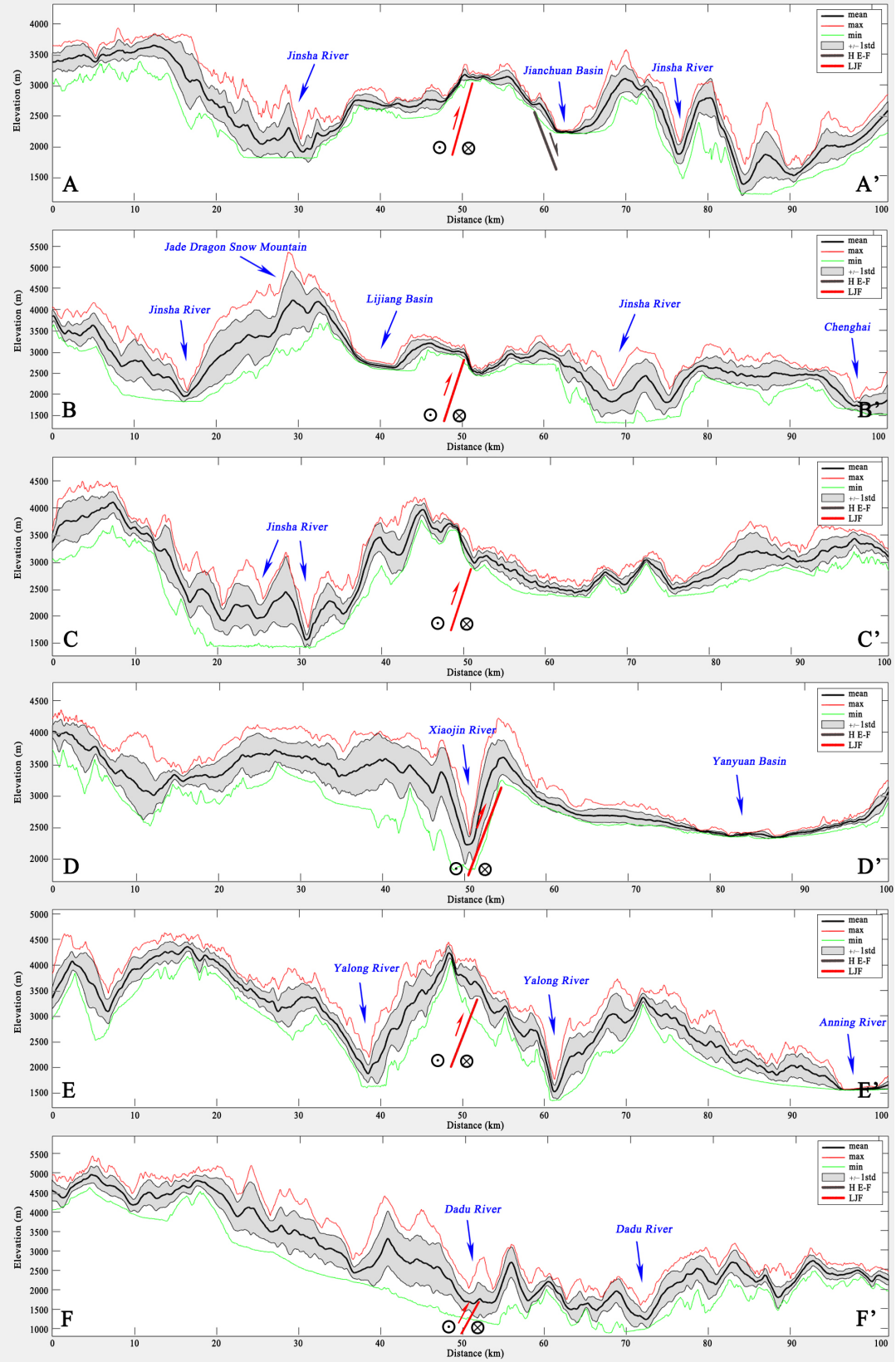

Figure 8. The strip terrain profiles across the LJF. The location of (**A**,**A′**) to (**F**,**F′**) are shown in Figure 1. The thick red line accompanied by an upward arrow signifies a reverse fault, whereas the thick grey line with a downward arrow denotes a normal fault. The circles containing a dot on the left side and a cross on the right side indicate that the fault is a left-lateral strike–slip fault.

5. Discussion

In active tectonic areas, fault activity controls landform evolution. However, the landform evolution process is also affected by the combined effects of climate, lithology, etc. When using landforms to reflect the response of tectonics, the influence of external factors such as climate and lithology must be considered. Then, the dominant factors controlling the landform evolution of a certain region can be analyzed [65].

5.1. Climatic Factors

The climate, which plays a role through precipitation, is an important factor affecting the development of geomorphology. Precipitation affects river flow, which determines the river's ability to erode, transport, and deposit, thus affecting the evolution of watersheds [66]. When other factors remain unchanged, the greater the watershed precipitation, the faster the landform evolution, and the smaller the corresponding values of geomorphic indices such as slope, RDLS, HI, and k_{sn}. Precipitation is negatively correlated with geomorphic indices. The AAP of each sub–watershed was obtained via spatial analysis (Figure 9). The detailed values are shown in Supplementary Materials.

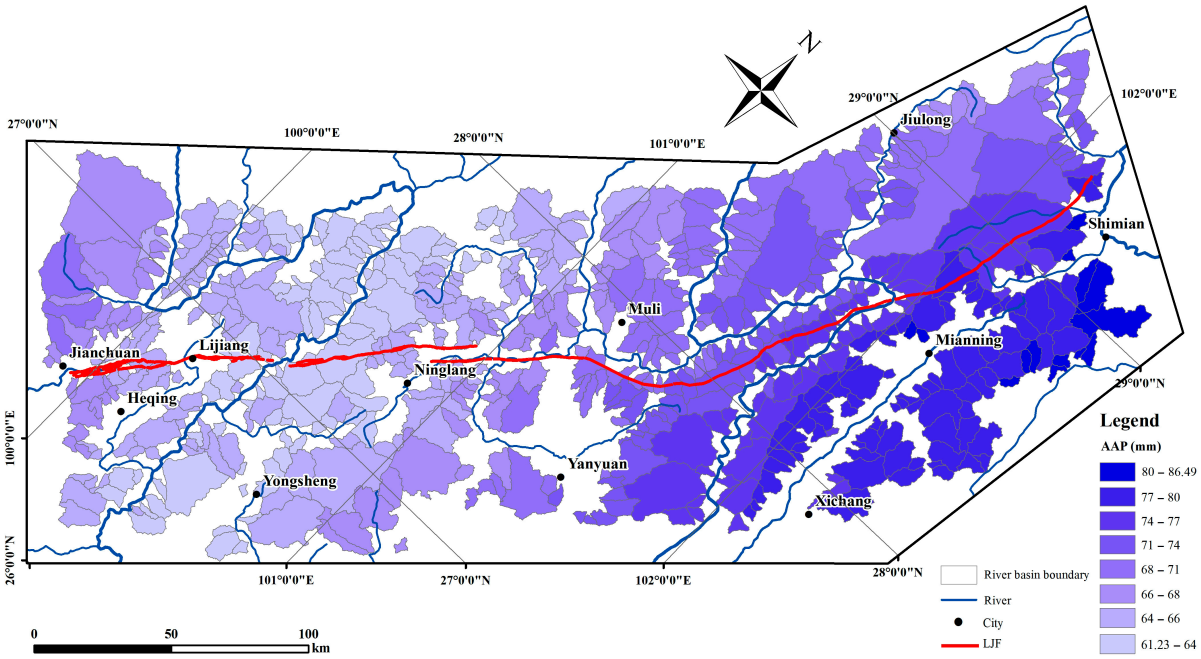

Figure 9. The spatial distribution of AAP in the sub–watersheds around the LJF from 2000 to 2022.

The study area is affected by the South Asian and Southeast Asian monsoons (Figure 9). The precipitation gradually increases from the northeast and southwest corners around the LJF to the center. Compared with the results of the geomorphic indices in this work, the precipitation on the southeast side of the LJF is generally higher than that on the northwest side, which is exactly the opposite of the trend of the geomorphic indices. Furthermore, the precipitation in the northeast along the LJF is significantly higher than in the southwest, the same as the trend of the geomorphic indices. This negates the view that precipitation controls the geomorphic evolution in the study of the LJF. In addition, this work also included Spearman correlation analysis using geomorphic indices and the AAP and RH of 593 sub–watersheds, and the results are shown in Figure 10. The results show that AAP positively correlates with slope and RDLS has no correlation with k_{sn}. AAP is only negatively correlated with HI, and the correlation is very small. This further confirms that AAP is not the main factor affecting the geomorphic evolution around the LJF.

Figure 10. The Spearman correlation between geomorphic indices (slope, RDLS, HI, k_{sn}), AAP, and RH in the sub–watersheds of the LJF. Note: ** and * denote significance at the 0.01 and 0.05 probability levels, respectively.

5.2. Lithology

The hardness of the rock directly affects the erosion resistance of the bedrock river. In general, hard rocks have strong erosion resistance, while soft rocks have weak erosion resistance [67]. When other conditions are the same, the higher the RH, the greater the slope, RDLS, HI, and k_{sn} corresponding to the area, and conversely for smaller values of the geomorphic indices. The RH is positively correlated with the geomorphic indices [36].

The hardness of bedrock is related to many factors [68]. Currently, the hardness of rocks can be measured by the Schmidt rebound hammer [14]. The hardness of bedrock is expressed by the rebound distance R. The larger the R value, the stronger the RH and the greater the ability to resist plastic deformation. This method has been widely used in geomorphology [37,69], rock mechanics engineering exploration, and other research areas [70]. Since the study area is too large and field measurements are very difficult, this study refers to the grading score table obtained by previous researchers based on Selly's [71] bedrock corrosion resistance scoring method [72]. This work uses two indicators of rock hardness and weathering degree in the table, with full marks of 25 and 12 points, respectively. RH is divided into five levels based on the *Handbook of Engineering Geology* (fifth edition) and previous research experience [37]. The degree of weathering is roughly assumed to be related to the age of the rock. The older the rock, the higher the degree of weathering and the lower the hardness value. Quaternary deposits are classified as very soft rocks with a hardness of 5, regardless of their degree of weathering. Based on the lithology and age data of rocks in the 1:2.5 million geological maps of China [33] (Figure 11), the spatial distribution of RH and the average RH of the sub–watersheds around the LJF is obtained.

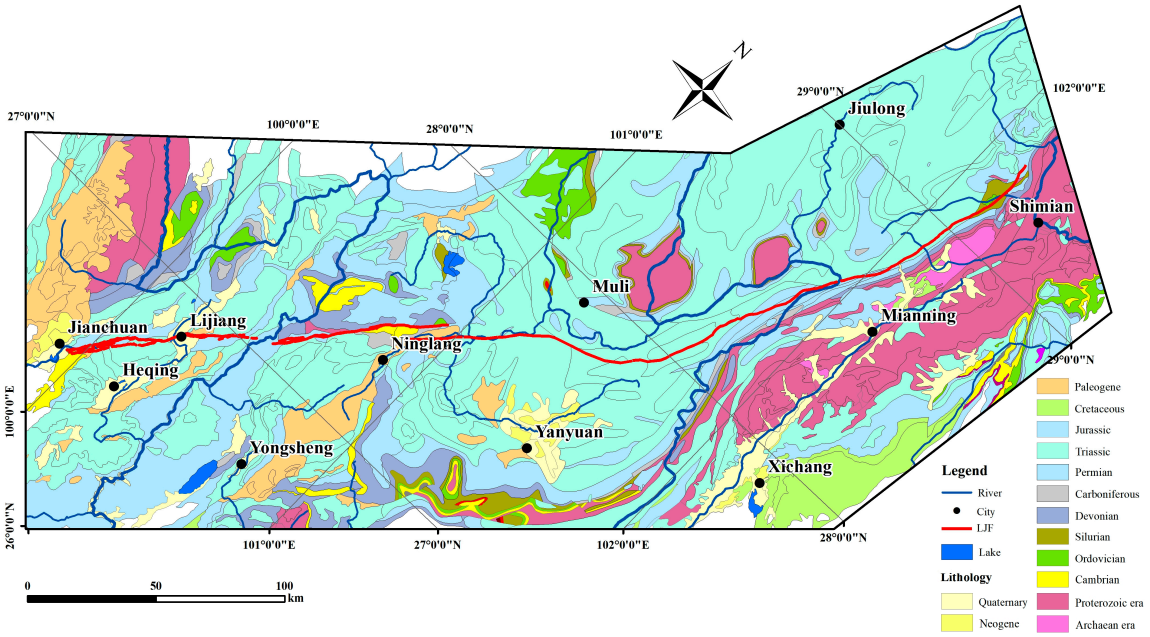

Figure 11. The spatial distribution of strata around the LJF.

Figure 12 shows that the RH is high in the areas around Yongsheng, Ninglang, and Yanyuan. Still, compared with the results of the spatial distribution of geomorphic indices in the previous text, the values of the slope, RDLS, HI, and k_{sn} are all low in this area. The area between Jiulong and the LJF is a low–value area of RH, but the geomorphic indices value of this area are very high. However, there are also some areas, such as the bend of the Yalong River on the west of Xichang, where the RH positively correlates with the geomorphic indices. However, according to the results of Spearman correlation analysis, there is no correlation between the geomorphic indices and RH (Figure 11). Therefore, based on the results of the regional comparison and Spearman correlation analysis, rock erodibility is not the dominant factor controlling the geomorphic evolution around the LJF.

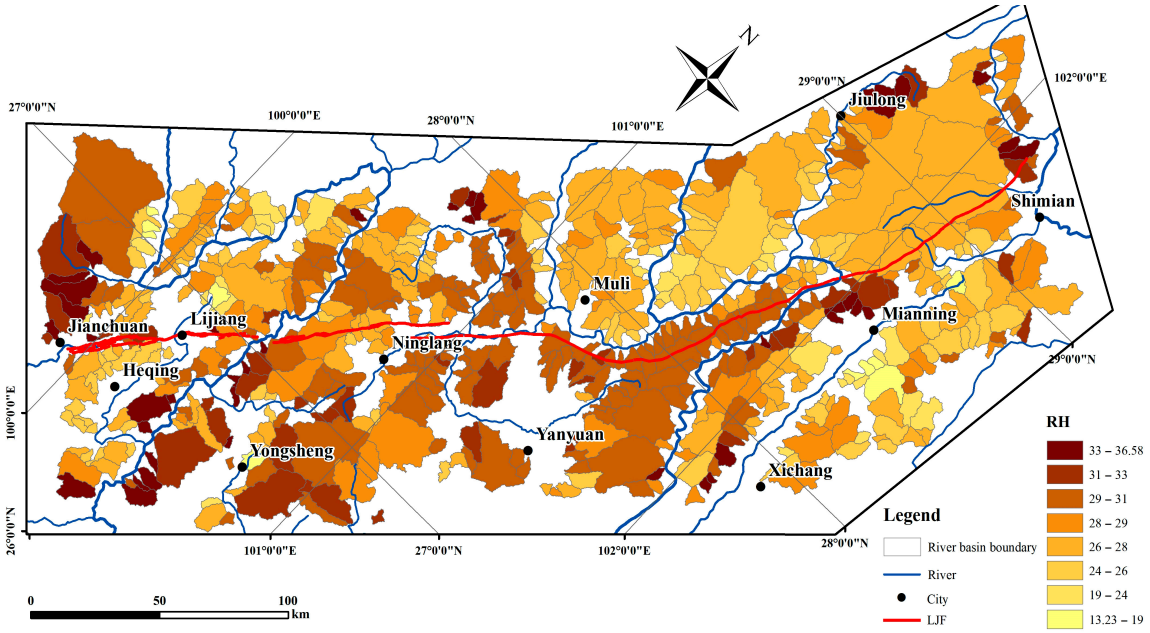

Figure 12. The spatial distribution of the average RH in the sub–watersheds around the LJF.

5.3. Tectonics

Taking Jianchuan at the southern end of the LJF as the starting point, the geomorphic indices of the sub–watersheds are projected onto the G–G′ line in Figure 2 along the fault direction to obtain a scatter plot of the geomorphic indices on both sides of the LJF. Since the data points are relatively scattered, a comparison chart of the geomorphic indices on both sides of the LJF is obtained after linear fitting of the data (Figure 13).

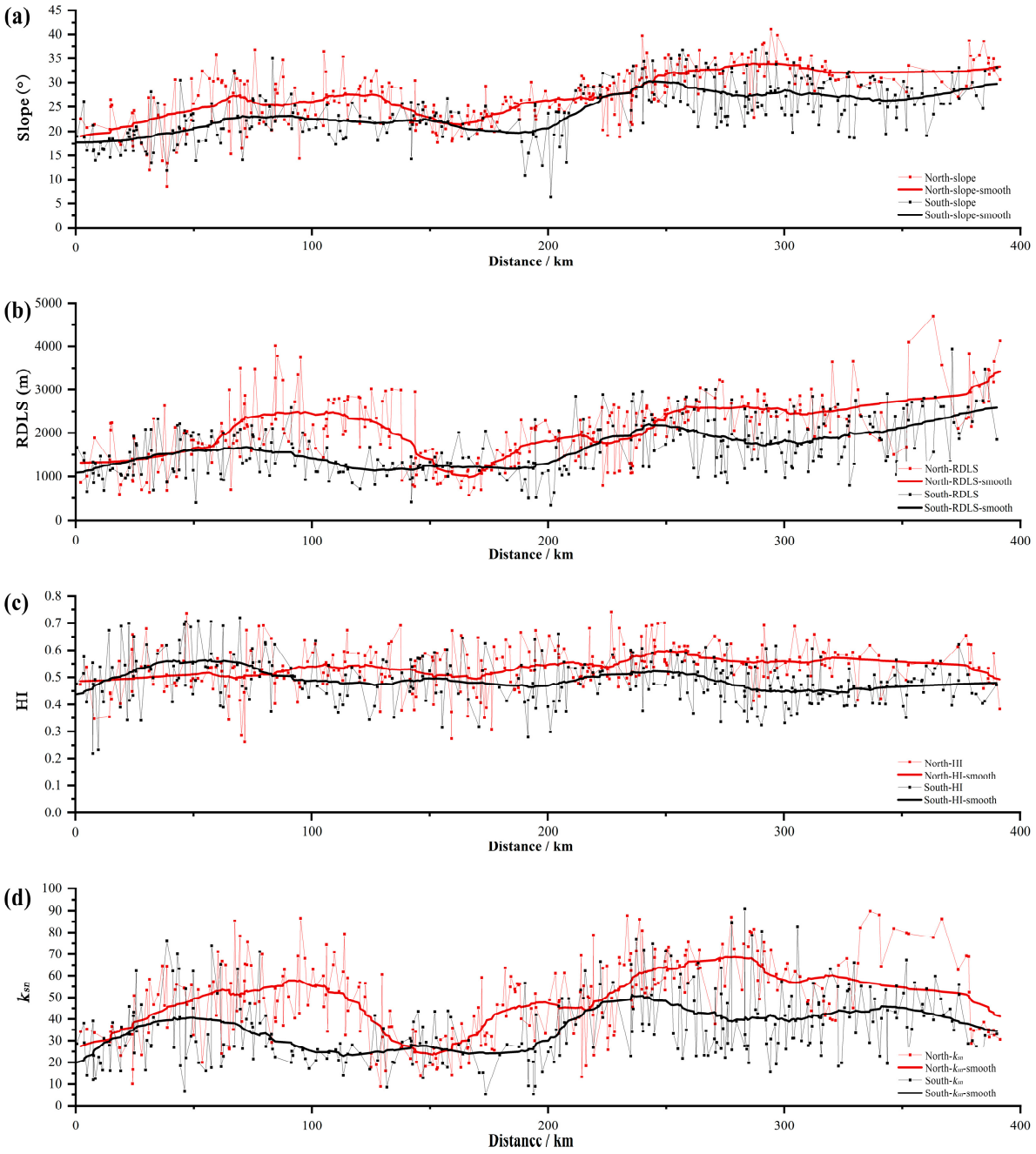

Figure 13. The geomorphic indices (slope (**a**), RDLS (**b**), HI (**c**), k_{sn} (**d**)) from southwest to northeast in the sub–watersheds on both sides of the LJF.

In Figure 13, there are significant differences in the geomorphic indices on both sides of the LJF. Overall, the geomorphic indices on the northwest side of the LJF are higher than those on the southeast side, and the variation trends of the slope, RDLS, and k_{sn} are also very similar, all increasing from southwest to northeast along the fault direction. In

addition, the slope, RDLS, and k_{sn} increase significantly at about 230 km. This coincides with the previous division of the LJF into the northeastern and middle sections based on this point [16,19]. The HI on the northwest side of the LJF also shows an increasing trend from southwest to northeast, but the amplitude is lower than that of other geomorphic indices. At 230 km, the HI on the northwest side of the LJF also increased significantly, while the HI on the southeast showed no obvious variation trend. This may be because the HI responds more significantly to landform uplift and less to landform subsidence.

An interesting phenomenon is that in the section of 0–70 km, the slope, RDLS, and k_{sn} are relatively close or not much different on both sides of the LJF, indicating that the vertical activity component of the LJF in this section is weak, and strike–slip movement is the main activity. This is also confirmed in the trenches in our recent and previous works [17,29]. However, the HI shows an obvious reversal in this section; that is, the HI on the southeast side of the LJF is significantly greater than that on the northwest. There may be two reasons for this phenomenon. One is that the dip of the LJF in this section has changed, and the southeast side has risen while the northwest side has fallen, but this assumption is contrary to the results of strip terrain profiles, slope, RDLS, and k_{sn}. Another hypothesis is that a fault nearly parallel to the LJF developed in the southeast, which undertook the vertical activity component and caused the relative uplift of the landform in the southeast. In fact, the Heqing–Eryuan fault (H–E F) is nearly parallelly developed at 10–15 km from the southeast side of the LJF fault (Figure 1). Therefore, if other factors that affect the spatial distribution of geomorphic indices are not considered, the geomorphic indices along the fault not only reflect the difference in uplift rates on both sides of the LJF and the trend of activity variation along the fault but the mutation position of the geomorphic indices value also indicates the segmentation of the fault.

We simplified Figure 13, retaining only the fitted line, and superimposed the lines to obtain a more intuitive comparison of the geomorphic indices on both sides of the LJF (Figure 14). The dotted box in Figure 14 shows that the four geomorphic indices all showed mutations at 70 km, 160 km, and 230 km. According to the above discussion, the geomorphic indices have a certain indicative effect on the fault segmentation. We used the mutation zone as the segmentation point and divided the LJF into four sections: the Jianchuan–Lijiang section, Lijiang–Ninglang section, Ninglang–Muli section, and Muli–Shimian section. In the Jianchuan–Lijiang section, as discussed above, the geomorphic indices on both sides of the LJF are close or not much different, and the fault is mainly characterized by strike–slip movement. In the north of Lijiang, the Lijiang Basin, which is about 6 km wide, separates the Jianchuan–Lijiang section and the Lijiang–Ninglang section, which may be a rupture stepover between the two sections. Previous studies on paleoearthquakes in the southwest and middle sections of LJF [16,17] showed that the paleoearthquake sequences in these two sections could not be compared. The Lijiang Basin was indeed a ruptured stepover of LJF. In the Lijiang–Ninglang section, the four geomorphic indices on the northwest side of the LJF are significantly higher than those on the southeast, indicating strong vertical activity in this section of the fault; in the north of Ninglang, the LJF is geometrically divided into two branches, with a distance of about 6 km between the two branches. This may be the stepover between the Lijiang–Ninglang section and Ninglang–Muli section, which caused a sudden change in the geomorphic indices. In the Ninglang–Muli section, the four geomorphic indices differ significantly on both sides of the LJF, but the values of the indices are lower than those in the adjacent sections, indicating that the fault activity in this section is relatively weakened. North of Muli, the geomorphic indices show a consistent mutation that causes the segmentation of the Ninglang–Muli section and Muli–Shimian section. This may be due to the strike of the LJF changes from NE to NNE at this point. In the Muli–Shimian section, the vertical activity of the fault is significantly enhanced.

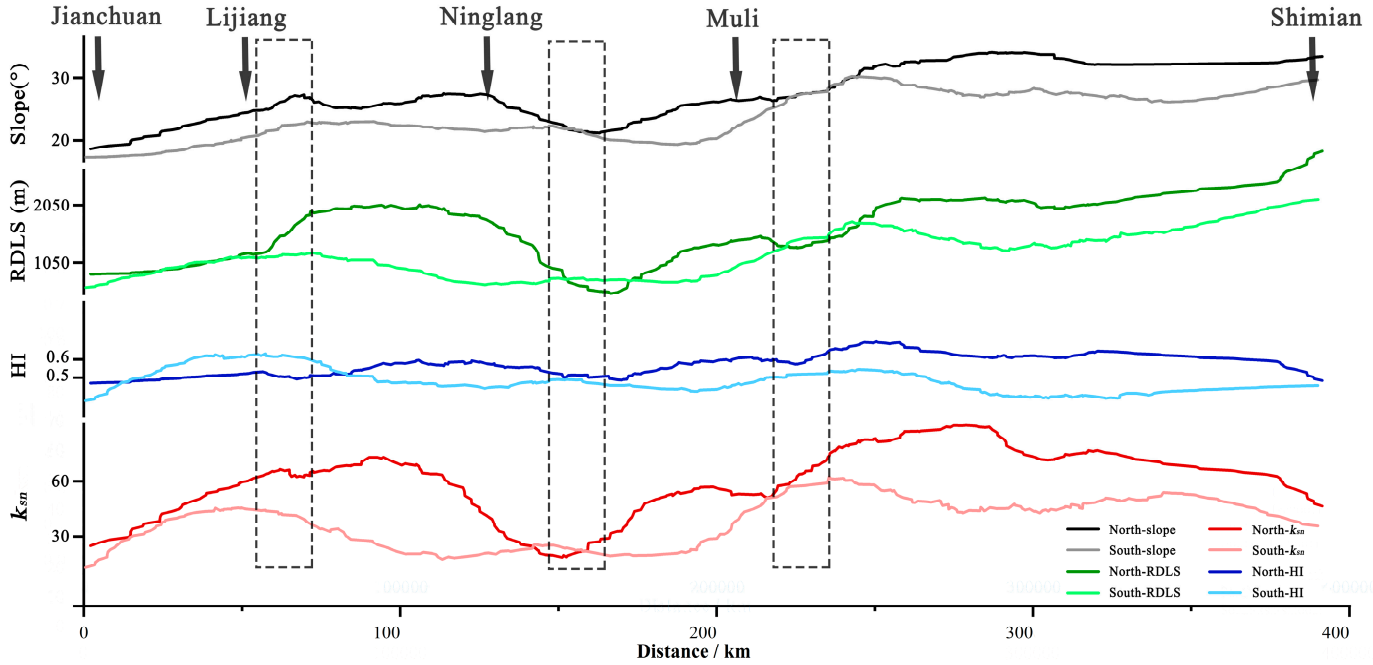

Figure 14. A comparison of geomorphic indices on both sides of the LJF.

Geological studies have shown that the average extrusion rate of the Sichuan–Yunnan rhombic block southeast of the Tibet Plateau decreases from the rear edge and middle to the front edge in the SE direction, which is mainly related to the thrust shielding effect of the LJF [21]. The results of this work also verify this point. The values of the slope, RDLS, HI, and k_{sn} in the southeast of the LJF are significantly smaller than those in the northwest. The six strip profiles perpendicular to the fault also have obvious vertical height difference responses at the fault. In addition, previous studies have found that the LJF absorbed about one–third of the left–lateral strike–slip deformation transmitted to the southeast by the Xianshuihe fault, resulting in the sum of the strike–slip rate of the Anninghe, Zemuhe, and Xiaojiang fault zones being significantly lower than that of the Xianshuihe fault [4]. We summarized the vertical and left–lateral strike–slip rates of the LJF obtained from previous geological research (Table 2). The left–lateral strike–slip rates of the southwestern section of the LJF (south of the Lijiang Basin) and the middle section (Lijiang to Muli) are not much different. Still, the vertical slip rates of the middle section are significantly higher than those of the southwest. The geological slip rate results are consistent with the trend of the geomorphic indices, which are low in the southwest and high in the northeast. Although there is a lack of vertical slip rate data for the northeast section of the LJF, it can be inferred from the geomorphic indices that the slip rate in the northeast section is higher than that in the southwest and middle sections. The geodetic results also show that the vertical activity of the LJF decreases from northeast to southwest [73,74], which is consistent with the results of geology and this work.

Based on the above analysis, the LJF is the dominant factor controlling the geomorphic evolution around the LJF. The vertical activity of the fault causes the geomorphic tectonic uplift on the northwest side of the LJF to be higher than that on the southwest side, and the results of the geomorphic indices and strip profiles also show the same characteristics. At the same time, fault activity geomorphic indices also decrease from northeast to southwest. The results of tectonic geomorphology and geology are consistent with each other, proving the rationality of the results of this work.

Table 2. The slip rate of the LJF in the south of Muli obtained from previous geological research.

Segments	Sites	Left–Lateral Strike–Slip (mm/a)	Vertical Slip Rate (mm/a)	Reference
Southwestern segment	Jianchuan	0.7 ± 0.2	0.2	[29]
	↓	3.8		[21]
		2.37 ± 0.2		[19]
		3.1 ± 0.4	0.15 ± 0.05	[23]
	Lijiang	3.7		[21]
		3.5 ± 0.8	0.2 ± 0.02	[29]
Middle segment		4.5 ± 0.2	0.65 ± 0.14	[23]
		3.1–4.3		[29]
		3.3	1–1.3	[21]
	↓	3.5	1.5–1.75	[21]
		3.7–4.8	0.55 ± 0.03	[29]
		0.9–2.4		[29]
		3.23 ± 0.22	0.35 ± 0.02	[19]
		3 ± 0.3	0.33 ± 0.04	[29]
	Muli	2.5		[29]

6. Conclusions

The purpose of this study is to evaluate the response of geomorphic indices to LJF activity. Based on a DEM, this study used ArcGIS in combination with MATLAB to obtain the spatial distribution of the slope, RDLS, HI, and k_{sn} of 593 sub–watersheds on the southeast and northwest sides of the LJF. Combining the results of the two methods, we studied the response of the geomorphology in the area around the LJF to the fault activity and analyzed the spatial differences in the activity of the LJF. The results show the following:

(1) The spatial distribution of climate and lithology have no significant correlation with the spatial distribution of geomorphic indices. The results of Spearman correlation analysis also further revealed no correlation among the three. This study shows that climate and lithology are not the controlling factors of the geomorphic evolution around the LJF.

(2) Tectonic activity is the dominant factor controlling the geomorphic evolution around the LJF, and the geomorphic indices convey the tectonic information of the LJF. The spatial distribution of the geomorphic indices reflects that the uplift of the northwest side of the LJF caused by the vertical activity of the LJF is higher than that of the southeast side and reveals that the vertical activity along the fault direction from northeast to southwest shows a gradual declining trend. In addition, with the north of Muli as the boundary, the geomorphic indices of the sub–watersheds in the northeast of Muli are significantly higher than those in the south, indicating that the LJF is segmented at this location. Taking the north side of the Lijiang basin as the boundary, the geomorphic indices show the change in fault activity pattern, confirming the rationality of the Lijiang basin as a stepover, which is consistent with the results of geological research. The Ninglang–Muli section is divided by the indices of the mutation zone, which corresponds to the geometric distribution and tectonic transition of the LJF on the north side of Ninglang.

(3) The elevation of the strip terrain profiles in the northwest direction of the LJF is significantly greater than in the southeast direction, and there is an obvious vertical activity response at the LJF. The average elevation of the profile from southwest to northeast constantly increases. The results of the strip terrain profiles verify the rationality of the results of the geomorphic indices.

(4) The results of tectonic geomorphology in this study are consistent with those of geology and geodesy in previous studies conducted by other researchers, which indicates that the spatial distribution of geomorphic indices can be used to indicate the variation trends of differential uplift and tectonic rates caused by fault activity.

This work provides evidence of the activity and segmentation of the LJF in tectonic geomorphology. The results also provide insight for the discussion of tectonic deformation and earthquake disaster mechanisms in the southeastern margin of the Tibet Plateau.

Supplementary Materials: The following are available online at https://www.mdpi.com/article/10.3390/rs16203826/s1.

Author Contributions: Conceptualization, R.D.; data curation, Y.C.; formal analysis, Y.C. and D.J.; funding acquisition, S.Z.; investigation, Y.C. and D.H.; methodology, R.D. and Y.C.; project administration, R.D.; resources, R.D.; software, Y.C.; supervision, R.D. and S.Z.; validation, Y.C.; visualization, Y.C. and L.L.; writing—original draft, Y.C. and R.D.; writing—review and editing, R.D. and Y.C. All authors have read and agreed to the published version of the manuscript.

Funding: This work was funded by the National Natural Science Foundation of China, grant number U2039201, and Research Grant from the National Institute of Natural Hazards, Ministry of Emergency Management of China, grant number ZDJ2020-12.

Data Availability Statement: The topography data are from https://e4ftl01.cr.usgs.gov/MEASURES/SRTMGL1.003/2000.02.11, accessed on 5 October 2023. The active fault data are from https://www.activefault-datacenter.cn/map, accessed on 10 October 2023. The earthquake catalog data are from https://data.earthquake.cn/datashare/report.shtml?PAGEID=earthquake_zhengshi, accessed on 10 November 2023. The regional lithologic data are from http://dcc.ngac.org.cn/geologicalData/cn//geologicalData/details/doi/10.23650/data.H.2017.NGA121474.K1.1.1, accessed on 1 November 2023.

Conflicts of Interest: The authors declare no conflicts of interest.

References

1. Molnar, P.H.; Tapponnier, P. Cenozoic tectonics of Asia: Effects of a continental collision. *Nature* **1975**, *189*, 419–426.
2. Qiao, X.; Wang, Q.; Du, R. Characteristics of current crustal deformation of active blocks in the Sichuan-Yunnan region. *Chin. J. Geophys.* **2004**, *47*, 805–811.
3. Wang, Y.; Shen, J.; Wang, Q.; Xiong, X. On the lateral extrusion of Sichuan-Yunnan block (Chuandian block). *Earth Sci. Front.* **2003**, *10*, 188–192.
4. Han, Z.; Xiang, H.; Guo, S. Sinistral shear and extension of the northern section of Lijiang Basin in northwest Yunnan in Quaternary. *Chin. Sci. Bulletin.* **2005**, *50*, 452–459. [CrossRef]
5. Yang, J.; Li, Y. *Principles of Geomorphology*, 3rd ed.; Peking University Press: Beijing, China, 2017.
6. Hack, J.T. Stream-profile analysis and stream-gradient index. *J. Res. Us Geol. Surv.* **1973**, *1*, 421–429.
7. Jaiswara, N.K.; Kotluri, S.K.; Pandey, P.; Pandey, A.K. MATLAB functions for extracting hypsometry, stream-length gradient index, steepness index, chi gradient of channel and swath profiles from digital elevation model (DEM) and other spatial data for landscape characterisation. *Appl. Comput. Geosci.* **2020**, *7*, 100033. [CrossRef]
8. Owen, L.A. 5.2 Tectonic Geomorphology: A Perspective. In *Treatise on Geomorphology*; Shroder, J.F., Ed.; Academic Press: San Diego, CA, USA, 2013; pp. 3–12.
9. Wobus, C.; Heimsath, A.; Whipple, K.; Hodges, K. Active out-of-sequence thrust faulting in the central Nepalese Himalaya. *Nature* **2005**, *434*, 1008–1011. [CrossRef]
10. Kirby, E.; Whipple, K. Quantifying differential rock-uplift rates via stream profile analysis. *Geology* **2001**, *29*, 415–418. [CrossRef]
11. Jing, L. Tectonic geomorphology, active tectonics and lower crustal channel flow hypothesis of the southeastern Tibetan Plateau. *Chin. J. Geol.* **2009**, *44*, 1227–1255.
12. Zhang, H.P.; Yang, N.; Liu, S.F.; Zhang, Y.Q. Recent progress in the DEM-based tectonogeomorphic study. *Geol. Bull. China* **2006**, *25*, 660–669.
13. Guo, L.; He, Z.; Li, L. Responses of Stream Geomorphic Indices to Piedmont Fault Activity in the Northern Segment of the Red River Fault Zone. *Remote Sens.* **2023**, *15*, 988. [CrossRef]
14. Li, X.; Zhang, H.; Su, Q. Bedrock channel form in the Madong Shan (NE Tibet): Implications for the strain transfer along the strike-slip Haiyuan Fault. *J. Asian Earth Sci.* **2019**, *181*, 103891–103896. [CrossRef]
15. Shen, K.; Dong, S.; Wang, Y. Active Tectonics Assessment Using Geomorphic and Drainage Indices in the Sertengshan, Hetao Basin, China. *Remote Sens.* **2023**, *15*, 3230. [CrossRef]
16. Ding, R.; Ren, J.; Zhang, S.; Lv, Y.; Liu, H. Late quaternary paleoearthquakes on the middle segment of the Lijiang-Xiaojinhe fault, southeastern Tibet. *Seismol. Geol.* **2018**, *40*, 622–640.

17. Li, A.; Zhang, S.; Ding, R.; Wang, X. A paleoseismic research of the south segment of the Lijiang-Xiaojinhe fault in the Holocene. *Bull. Inst. Crustal Dyn.* **2016**, *1*, 1–9.
18. Wang, Y.; Wang, E.; Shen, Z.; Wang, M.; Gan, W.; Qiao, X.; Meng, G.; Li, T.; Tao, W.; Yang, Y. GPS-constrained inversion of present-day slip rates along major faults of the Sichuan-Yunnan region, China. *Sci. China Ser. D: Earth Sci.* **2008**, *51*, 1267–1283. [CrossRef]
19. Cheng, J.; Xu, X.; Gan, W.; Ma, W.; Chen, W.; Zhang, Y. Block model and dynamic implication from the earthquake activities and crustal motion in the southeastern margin of Tibetan Plateau. *Chin. J. Geophys.* **2012**, *55*, 1198–1212.
20. Gao, Y.; Ding, R.; Zhang, S. Slip Rate of Lijiang-Xiaojinhe Fault in the Holocene. *Technol. Earthq. Disaster Prev.* **2019**, *14*, 617–627.
21. Xiang, H.; Xu, X.; Guo, S.; Zhang, W.; Li, H.; Yu, G. Inistral thrusting along the Lijiang-Xianjinhe fault since quaternary and its geologic-tectonic significance. *Seismol. Geol.* **2002**, *24*, 188–198.
22. Li, H.; Ding, R.; Zhang, S. Geomorphological features of the south and middle sections of Lijiang-Xiaojinhe fault and their tectonic significance. *Technol. Earthq. Disaster. Prev.* **2020**, *2*, 380–391.
23. Xu, X.; Wen, X.; Zheng, R.; Ma, W.; Song, F.; Yu, G. Pattern of latest tectonic motion and its dynamics for active blocks in Sichuan-Yunnan region, China. *Sci. China Ser. D Earth Sci.* **2003**, *46*, 210–226. [CrossRef]
24. Shen, Z.K.; Lü, J.; Wang, M.; Bürgmann, R. Contemporary crustal deformation around the southeast borderland of the Tibetan Plateau. *J. Geophys. Res. Solid Earth* **2005**, *110*, 1–17. [CrossRef]
25. Burchfiel, B.C.; Chen, Z. [Geological Society of America Memoirs] Tectonics of the Southeastern Tibetan Plateau and Its Adjacent Foreland. *Geol. Soc. Am. Bull.* **2013**, *1–15*, 1–164.
26. Pan, G.T.; Xu, Y.R.; Wang, P.S. The Cenozoic tectonics at the eastern margin of Qinghai-Xizang Plateau. In *Contribution to the Geology of the Qinghai-Xizang (Tibet) Plateau(12)–Tectonics in Sanjiang*; "Sanjiang"Monograph Editorial Committee, Ed.; Geology Press: Beijing, China, 1983; pp. 129–141.
27. Han, Z.; Guo, S.; Xiang, H.; Zhang, J.; Ran, Y. Seismotectonic environment of occurring the February 3, 1996 Lijiang M = 7.0 earthquake, Yunnan province. *Acta Seismol. Sin.* **2004**, *26*, 453–463. [CrossRef]
28. Wu, G. The modes and mechanism of quaternary fault movement in Lijiang-Dali area, northwestern Yunnan and their influence on environment. *Quat. Sci.* **1992**, *12*, 265–276.
29. Zhang, S.; Ding, R.; Ren, J.; Li, A.; Lv, Y.; Wang, X.; Li, T.; Liu, S.; Zhao, L.; Liu, H. *Description of Lijiang-Xiaojinhe Active Fault (1:50,000)*; Seismological Press: Beijing, China, 2019.
30. Rabus, B.; Eineder, M.; Roth, A.; Bamler, R. The shuttle radar topography mission—A new class of digital elevation models acquired by spaceborne radar. *Isprs-J. Photogramm. Remote Sens.* **2003**, *57*, 241–262. [CrossRef]
31. van Zyl, J.J. The Shuttle Radar Topography Mission (SRTM): A breakthrough in remote sensing of topography. *Acta Astronaut* **2001**, *48*, 559–565. [CrossRef]
32. Peng, S. *1-km Monthly Mean Temperature Dataset for China (1901–2022)*; National Tibetan Plateau Data Center: Beijing, China, 2024.
33. Ye, T.; Huang, C.; Deng, S. 1:2.5 million spatial database of digital geological maps of the People's Republic of China. *Geol. China* **2017**, *44*, 19–24.
34. Kirby, E.; Whipple, K.X.; Tang, W.; Chen, Z. Distribution of active rock uplift along the eastern margin of the Tibetan Plateau: Inferences from bedrock channel longitudinal profiles. *J. Geophys. Res. Solid Earth* **2003**, *108*, 1–24. [CrossRef]
35. Stock, J.; Dietrich, W.E. Valley incision by debris flows: Evidence of a topographic signature. *Water Resour. Res.* **2003**, *39*, 1–25. [CrossRef]
36. Li, Q.; Pan, B.; Gao, H.; Wen, Z.; Hu, X. Differential rock uplift along the northeastern margin of the Tibetan Plateau inferred from bedrock channel longitudinal profiles. *J. Asian Earth Sci.* **2019**, *169*, 182–198. [CrossRef]
37. Liang, O.; Ren, J.; Lü, Y. The response of fluvial geomorphologic characteristics of the Fujiang drainge basin to activity of the Huya Fault zone. *Seismol. Geol.* **2018**, *40*, 42–56.
38. Scherler, D.; Bookhagen, B.; Strecker, M.R. Tectonic control on10 Be-derived erosion rates in the Garhwal Himalaya, India. *J. Geophys. Res. Earth Surf.* **2014**, *119*, 83–105. [CrossRef]
39. Schmidt, K.M.; Montgomery, D.R. Limits to relief. *Science* **1995**, *270*, 617–620. [CrossRef]
40. Ouimet, W.B.; Whipple, K.X.; Granger, D.E. Beyond threshold hillslopes; channel adjustment to base-level fall in tectonically active mountain ranges. *Geology* **2009**, *37*, 579–582. [CrossRef]
41. Whipple, K.X.; Kirby, E.; Brocklehurst, S.H. Geomorphic limits to climate-induced increases in topographic relief. *Nature* **1999**, *401*, 39–43. [CrossRef]
42. Whipple, K.X.; Tucker, G.E. Dynamics of the stream-power river incision model: Implications for height limits of mountain ranges, landscape response timescales, and research needs. *J. Geophys. Res. Solid Earth* **1999**, *104*, 17661–17674. [CrossRef]
43. Tu, H.; Liu, Z. Study on relief amplitude in China. *Acta Geod. Cartogr. Sin.* **1991**, *20*, 311–319.
44. Wang, L.; Tong, X.J. Analysis on relief amplitude based on change point method. *Geogr. Geo-Inf. Sci.* **2007**, *23*, 15.
45. Zhang, W.; Li, A.N. Study on the optimal scale for calculating the relief amplitude in China based on DEM. *Geogr. Geo-Inf. Sci.* **2012**, *28*, 8–12.
46. Zhong, J.; Lu, T. Optimal statistical unit for relief amplitude in Southwestern China. *Bull. Soil Water Conserv.* **2018**, *38*, 175–181.
47. Strahler, A.N. Hypsometric (area-altitude) analysis of erosional topography. *Geol. Soc. Am. Bull.* **1952**, *63*, 1117–1142. [CrossRef]
48. Davis, W.M. The Geographical Cycle. In *Climatic Geomorphology*; Derbyshire, E., Ed.; Macmillan Education UK: London, UK, 1973; pp. 19–50.
49. Pérez-Peña, J.V.; Azor, A.; Azañón, J.M.; Keller, E.A. Active tectonics in the Sierra Nevada (Betic Cordillera, SE Spain): Insights from geomorphic indexes and drainage pattern analysis. *Geomorphology* **2010**, *119*, 74–87. [CrossRef]

50. Pike, R.J.; Wilson, S.E. Elevation-relief ratio, hypsometric integral, and geomorphic area-altitude analysis. *Geol. Soc. Am. Bull.* **1971**, *82*, 1079–1083. [CrossRef]
51. Perron, J.T.; Royden, L. An integral approach to bedrock river profile analysis. *Earth Surf. Process. Landf.* **2013**, *38*, 570–576. [CrossRef]
52. Goren, L.; Fox, M.; Willett, S.D. Tectonics from fluvial topography using formal linear inversion: Theory and applications to the Inyo Mountains, California. *J. Geophys. Res. Earth Surf.* **2014**, *119*, 1651–1681. [CrossRef]
53. Flint, J.J. Stream Gradient as a Function of Order, Magnitude, and Discharge. *Water Resour. Res.* **1974**, *10*, 969–973. [CrossRef]
54. Kirby, E.; Whipple, K.X. Expression of active tectonics in erosional landscapes. *J. Struct. Geol.* **2012**, *44*, 54–75. [CrossRef]
55. Fielding, E.; Isacks, B.; Barazangi, M.; Duncan, C. How flat is Tibet? *Geology* **1994**, *22*, 163–167. [CrossRef]
56. Fielding, E.J. Tibet uplift and erosion. *Tectonophysics* **1996**, *260*, 55–84. [CrossRef]
57. Liang, M.J.; Zhou, R.J.; Yan, L.; Zhao, G.H.; Guo, H.M. The relationships between neotectonic activity of the middle segment of Dari fault and its geomorphological response, Qinghai Province, China. *Seismol. Geol.* **2014**, *36*, 28–38.
58. Su, Q.; Liang, M.; Yuan, D.; Xie, H.; Wu, Z. Geomorphic features of the Bailongjiang river drainage basin and its relationship with geological disaster. *Earth Sci.* **2016**, *41*, 1758–1770.
59. Xu, S.; Liu, Y. Associations among ecosystem services from local perspectives. *Sci. Total Environ.* **2019**, *690*, 790–798. [CrossRef] [PubMed]
60. Wu, Z.; Zhang, Y.; Hu, D.; Zhao, X.; Ye, P. Late Quaternary normal faulting and its dynamic mechanism of the Haba-Yulong east piedmont, northwest Yunnan. *Sci. China D* **2008**, *38*, 1361–1375.
61. Yin, G.; Su, G.; Ding, R.; Han, F.; Li, G.; Cheng, L.; Yang, G.; Wang, D. Kinematic property of the eastern piedmont fault of Yulong Mountains and its implication for geomorphology in Yunnan, southwest of China. *Quat. Sci.* **2017**, *37*, 250–259.
62. Smith, A.G.G.; Fox, M.; Schwanghart, W.; Carter, A. Comparing methods for calculating channel steepness index. *Earth-Sci. Rev.* **2022**, *227*, 103970. [CrossRef]
63. Schwanghart, W.; Kuhn, N.J. TopoToolbox: A set of Matlab functions for topographic analysis. *Environ. Modell. Softw.* **2010**, *25*, 770–781. [CrossRef]
64. Schwanghart, W.; Scherler, D. Short Communication: TopoToolbox 2–MATLAB-based software for topographic analysis and modeling in Earth surface sciences. *Earth Surf. Dyn.* **2014**, *2*, 1–7. [CrossRef]
65. Kuehnl, A.; Pfiffner, O.A. The relief of the Swiss Alps and adjacent areas and its relation to lithology and structure; topographic analysis from a 250-m DEM. *Geomorphology* **2001**, *41*, 285–307.
66. Chen, H.; Byun, J. Effects of erosional resistance on bedrock channel occurrence and morphology: Examination of the Seo River catchment in South Korea. *Geomorphology* **2023**, *438*, 108810. [CrossRef]
67. Sklar, L.S.; Dietrich, W.E. Sediment and rock strength controls on river incision into bedrock. *Geology* **2001**, *29*, 1087–1090. [CrossRef]
68. Li, Q.; Qin, B.; Pan, B. Bedrock channel width responses to tectonic uplift and lithologic resistance in the northern Qilian Mountains. *Quat. Sci.* **2020**, *40*, 132–147.
69. Spotila, J.A.; Moskey, K.A.; Prince, P.S. Geologic controls on bedrock channel width in large, slowly-eroding catchments: Case study of the New River in eastern North America. *Geomorphology* **2015**, *230*, 51–63. [CrossRef]
70. Kovler, K.; Wang, F.; Muravin, B. Testing of concrete by rebound method: Leeb versus Schmidt hammers. *Mater. Struct.* **2018**, *51*, 1–14. [CrossRef]
71. Selby, M.J. A rock mass strength classification for geomorphic purpose: With tests from Antarctica and New Zealand. *Z. Für Geomorphol.* **1980**, *24*, 31–51. [CrossRef]
72. Qin, B.; Li, Q.; Pan, B.; Wu, J.; Ji, X.; Chen, T. Evaluation of bedrock corrosion resistance and its influence on channel width in eastern Qilian Mountains. *Quat. Sci.* **2021**, *41*, 14–27.
73. Li, Y.; Hao, M.; Ji, L.; Qin, S. Fault slip rate and seismic moment deficit on major active faults in mid and south part of the Eastern margin of Tibet plateau. *Chin. J. Geophys.* **2014**, *57*, 1062–1078.
74. Zhu, S.; Yang, G.; Liu, X.; Dang, X. The deformation characteristics of Sichuan-Yunnan region in recent period. *Geomat. Inf. Sci. Wuhan Univ.* **2017**, *42*, 1765–1772.